Compendium of Computer Science
ISSN Print: 3079-5362
ISSN Online: 3079-5370
https://doi.org/10.63313/CS.8005

Surface Defect Detection of Corrugated Sheets Based on Photometric Stereo Vision

Jiannan Zhang*. Shaoli Li
School of Information Science And Engineering, Shenyang University of Technology, Shenyang, China
Email: zjn@smail.sut.edu.cn

How to cite this paper: Zhang, J., & Li, S. (2025). Surface Defect Detection of Corrugated Sheets Based on Photometric Stereo Vision. Compendium of Computer Science, 1(1), 54–65. ISSN Print: 3079-5362. ISSN Online: 3079-5370.
https://doi.org/10.63313/CS.8005
Published: 2025-04-17

Abstract

Plate heat exchangers are extensively employed in industrial processes for thermal energy transfer and waste heat recovery. The core component, the cor-rugated sheets, possesses a complex metallic surface geometry that is critical to the exchanger's performance. Corrugated sheets are formed through die stamp-ing, during which manufacturing defects may occur due to process limitations. Detecting defects prior to use is crucial for ensuring the safety of industrial op-erations. Due to the complex curved surface geometry of the corrugated sheets, images captured by a single-viewpoint imaging system often suffer from shading caused by the plate's undulating structure. As a result, defects tend to appear within shadowed regions of the surface, making it difficult to enhance their con-trast through illumination alone, thereby posing significant challenges for defect detection. The paper, based on photometric stereo vision, develops a photomet-ric stereo imaging system tailored for corrugated sheets and proposes a feature map extraction method based on Gauss spherical distance mean convolution. Based on the Gauss spherical distance feature map, defects are enhanced, and defect detection is performed using a method that fills the gray-scale concave segments of the feature map and marks the extrema points. Experimental results show that the defect detection accuracy in both the flow guide and heat ex-change regions of the corrugated sheets exceeds 95%.

Keywords

Photometric Stereo Vision; Plate Heat Exchanger Corrugated sheets; Machine Vision; Defect Detection

1. Introduction

Plate Heat Exchanger (PHE) is a heat transfer device with metal corrugated sheets (commonly referred to as "corrugated sheets" in the industry) as its core component. Heat exchange, condensation, evaporation, waste heat recovery, preheating, and cooling are achieved through the flow of gases and liquids with different temperatures in the flow channels on both sides of the corrugated sheets. PHEs are widely used in various fields, including national production, energy, power generation, and military industries [1]. As the core component of the PHE, the corrugated sheets are formed by cold stamping a metal flat plate, resulting in a surface with irregularly sized wave-like undulations. As shown in Figure 1, the structure of the corrugated sheets is generally divided into three main sections: the sealing groove area, which prevents liquid leakage between the plates; the flow guide area, which is used to evenly distribute gases/liquids; and the heat exchange area, which is responsible for heat transfer. The diversion zone is populated with several convex and concave structures, resembling rectangular or circular protrusions and recesses, while the heat exchange area consists of a series of parallel V-shaped corrugated structures [2]. The corrugated sheets are formed through cold stamping of substrates such as stainless steel, nickel-based alloys, and titanium alloys. During the stamping process, factors such as material stress, die wear, die heat treatment deformation, and the mechanical properties of the sheet material may lead to cracking. Defects are likely to occur at the edges of the stress points. Currently, no defects have been found on the flat surface; therefore, defects are expected to be present on the inclined surfaces of the corrugated sheets [3].

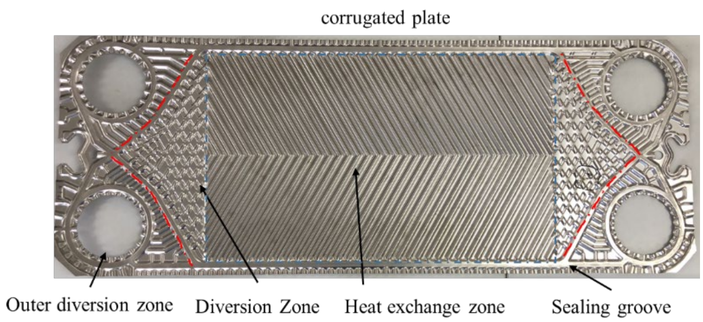

Figure 1. Structure of the Plate Heat Exchanger

2. Method

2.1. Design of Hardware System

The imaging system used in this study is a four-light source photometric stereo vision system [4]. As shown in Figure 2, commands sent from the host computer to the light source control circuit via serial communication. After decoding, the corresponding light sources are triggered to capture images, and this process is repeated four times to obtain a set of photometric stereo data. A white high-power coaxial point light source is selected, and the camera used is a flat-panel camera manufactured by XIMA, Germany, with a resolution of 1280×1024. A telecentric lens is chosen to maintain consistent magnification of points at different depths on the corrugated sheets in the image plane and to minimize distortion.

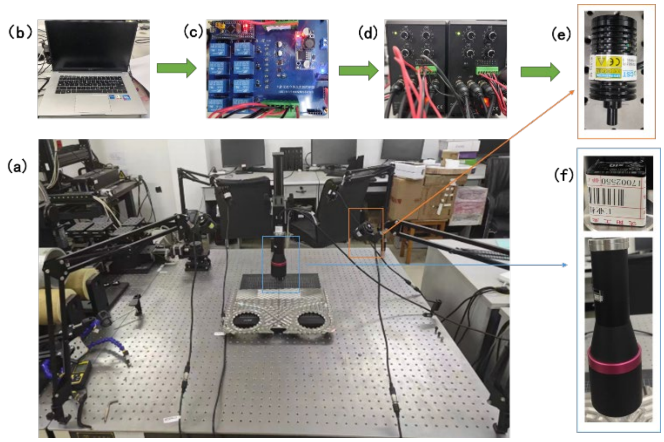

Figure 2. Hardware System

2.2. Calibration of Light Source Direction

When a distant point light source is used, it is assumed that the illumination reaching the surface of the corrugated sheets is parallel and uniform. Therefore, for each light source, a light source direction matrix needs to be determined. This paper utilizes a spherical object with specular reflection properties to calibrate the light source direction [5]. As shown in Figure 3, the light source direction is represented by L, N is the surface normal vector of the spherical object, and the viewing direction is V (0,0,1). The relationship between them is given by L = 2(N·V) N - V. Since V is known, L can be determined once N is known. N can be obtained from the known radius R of the specular black sphere and the geometric relationship of the light source illumination on its surface. The radius r can be calculated using image processing techniques, and z can be determined from r and R [6].

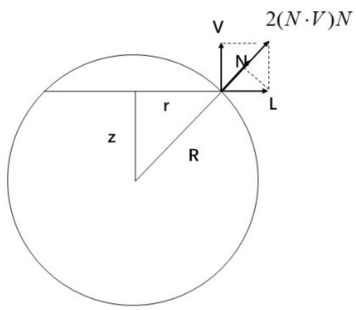

Figure 3. Schematic Diagram for Determining Light Source Direction

The light source calibration uses a 2 cm diameter obsidian sphere as the calibration object, and the light source directions are listed in Table 1.

Table 1. Light Source Direction Calibration Values

Light Source	Direction Vector
Light Source1	(0.3633, 0.4173, 0.8329)
Light Source 2	(-0.3731, 0.3928, 0.8405)
Light Source 3	(-0.3732, -0.3020, 0.8772)
Light Source 4	(0.3511 ,-0.3609, 0.8640)

2.3. Acquisition of Normal Vectors

The imaging system in this paper consists of a distant point light source, which can be regarded as uniform parallel light. According to Lambert's cosine law [7], the radiative flux reflected from a unit surface area into a unit solid angle in space is directly proportional to the cosine of the angle between the direction and the surface normal.

$$L = \rho \frac{E}{\pi} \cos\theta$$

Here, E represents the incident irradiance, L is the reflected luminance, and ρ denotes the surface reflectance. θ is the angle between the light source direction and the surface. The luminance reflected from the surface of the corrugated sheets to the camera is related to the angle between the light source direction and the surface. Therefore, the orientation of each pixel's corresponding microfacet is determined by utilizing multiple images and the constraint relationship with the light source direction [8]. As shown in Figure 4, the relationship between the image irradiance under a specific light source direction and the surface orientation can be expressed by the following equation:

$$I(x, y) = \rho \cos\theta_i = n \cdot s$$

Here, n is the surface normal vector, and s is the light source direction vector.

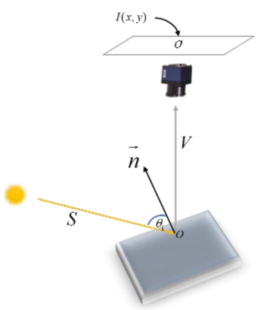

Figure 4. Photometric Stereo Vision Principle

The matrix form of the irradiance equations from multiple images is given by:

$$\begin{bmatrix} I_1 \\ I_2 \\ \vdots \\ I_n \end{bmatrix} = \rho \begin{bmatrix} S_1 \\ S_2 \\ \vdots \\ S_n \end{bmatrix} n$$

Here, S denotes the light source matrix, I represents the pixel intensity matrix, ρ denotes the surface reflectance, and n is the normal vector. By applying the least squares method to solve this overdetermined system of equations, the least-squares solution matrix m for the surface can be obtained using the following formula:

$$m = \left(S^T S\right)^{-1} S^{-1} I$$

Where the reflectance ρ is defined as:

$$\rho = |m|$$

Normal vector:

$$n = \frac{m}{|m|} = \frac{m}{\rho}$$

As shown in Figure 5, Figure 5a presents a set of grayscale images of the flow distribution zone captured under four different lighting directions. Figure 5b shows the calculated surface normal vectors, where the x, y, and z components are represented by the B, G, and R channels of the color image, respectively. Figure 5c displays the resulting reflectance map. Figure 6a illustrates a set of grayscale images of the heat exchange zone taken from four directions, Figure 6b shows the corresponding normal map, and Figure 6c depicts the reflectance map.

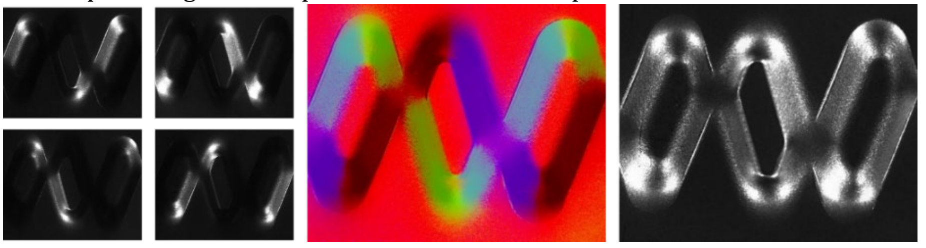

a Grayscale image set b Normal vector map c Reflectance map

Figure 5. Normal Vectors in the diversion zone

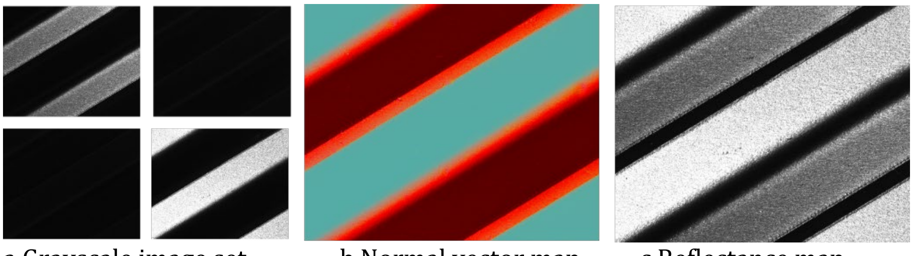

a Grayscale image set b Normal vector map c Reflectance map

Figure 6. Normal Vectors in the heat exchange zone

2.4. Extraction of Feature Map

To address the issue of low contrast in defect feature maps, this paper proposes a feature representation method based on Gaussian spherical distance mean convolution. The surface normal vectors obtained through photometric stereo are unit vectors. By placing the tails of these vectors at the center of a unit sphere—referred to as the Gauss sphere—this configuration provides an effective representation of surface orientation. Each normal vector terminates at a point on the surface of the Gauss sphere, and thus, the distribution of points on the Gauss sphere reflects the orientation characteristics of the surface [9]. Firstly, the mean vector m of the neighborhood is obtained by applying a mean convolution kernel to each of the three channels of the normal vector n.

$$m(x,y) = \sum_{-k}^{k}\sum_{-k}^{k}\sum_{-k}^{k} n(x+i, y+j)\cdot G(i,j)$$

Where n is the normal vector obtained through photometric stereo at the pixel corresponding to the coordinates (x,y), k is the size of the convolution kernel, G is the convolution kernel, and i and j represent the relative positions within the convolution kernel. The mean convolution kernel used is:

$$G = \frac{1}{(2k+1)^2}$$

Then, the spherical distance between the normal vector and the mean vector is calculated:

$$d_b(x.y) = \arccos\left(\frac{n(x,y)\cdot m(x,y)}{\|n(x,y)\|\cdot\|m(x,y)\|}\right)$$

Finally, the spherical distance $d_b(x.y)$ is normalized into a grayscale image:

$$I(x,y) = d_{norm}(x.y)\times 255 = \frac{d_b(x.y) - d_{\min}}{d_{\max} - d_{\min}}\times 255$$

The size of the convolution kernel's neighborhood affects the representation of defects. To emphasize the distinction between the defect and its surrounding area, the size of the convolution kernel's neighborhood should be larger than the maximum width of the defect. However, the kernel should not be too large, as an excessively large kernel would increase computation time. Therefore, considering the size of the defect and the image's pixel resolution, a 10×10 convolution kernel is chosen to compute the mean vector.

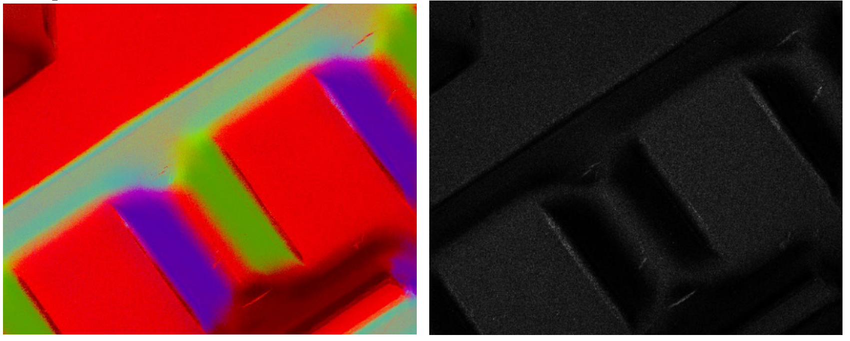

a Normal vectors with defects b Feature map based on spherical distance

Figure 7. Distance convolution feature map obtained using a 10×10 convolution kernel

2.5. Defect Detection Method

Since defects occur on the sloped surfaces and the edge variations in the feature map resemble defect features, it is necessary to eliminate the planar regions to obtain the region of interest (ROI) where defects exist. In the obtained normal vector map, the Z-direction component of planar vectors is close to 1. The Z-direction component nz of each vector is calculated, and those with nz >0.9 are considered planar regions. To remove some of the planar pixels near the boundary, a 10×10 convolution kernel is applied for erosion on the sloped surfaces, resulting in the final ROI. As shown in Figures 8 and 9, the localization results of the heat exchange zone and the diversion zone are presented, respectively.

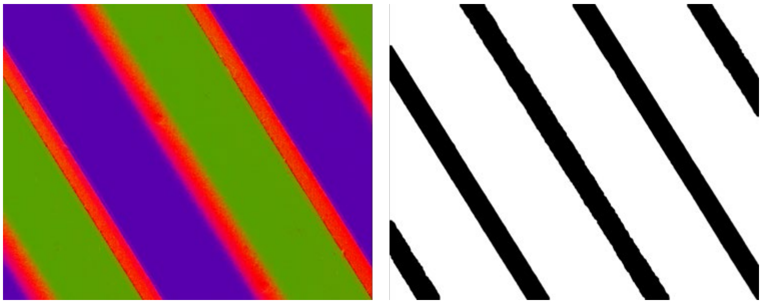

Figure 8. ROI localization result for the heat exchange area

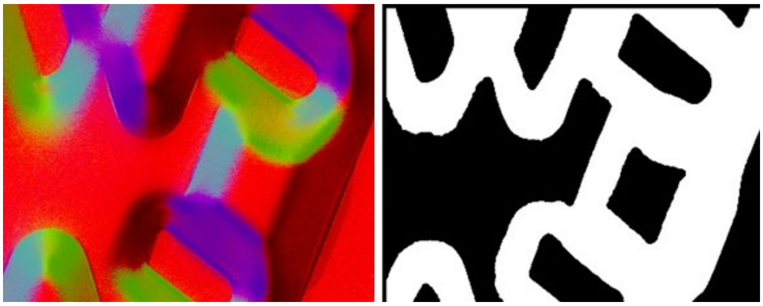

Figure 9. ROI localization result for the diversion area

As shown in Figure 10, the convex segments of the grayscale line within the region marked by the yellow line are truncated by the concave segments. Let the grayscale function of the one-dimensional grayscale defect represent the grayscale value $f(i)$ at point *i*. When the width of the convex and concave segments is 1, if $f(i) > f(i-1)$ and $f(i) > f(i+1)$, then $f(i)$ is a local maximum. If $f(i) < f(i-1)$ and $f(i) < f(i+1)$, then $f(i)$ is a local minimum. When the width of the convex and concave segments is 2, If $f(i) > f(i-2)$ and $f(i) > f(i+2)$, then both $f(i)$ and $f(i+1)$ are local maxima. Similarly, to achieve the filling of the concave segments, the concept of the magnitude of the extrema points needs to be introduced [10]. Since the convex and concave segments at both ends of the extrema are not symmetric, this paper defines the current grayscale value as the absolute magnitude of the current pixel. The difference between the local minimum and the larger of the two neighboring points is defined as the relative magnitude 1, denoted as $F1$, while the smaller difference is defined as the relative magnitude 2, denoted as F_2:

$$F_1 = \max(f(i-1), f(i+1)) - f(i)$$

$$F_2 = \min(f(i-1), f(i+1)) - f(i)$$

Firstly, for the first-order grayscale profile of the feature map, local minima with a width of 1 are raised by adding a value $F2$ to fill the concave segments with a width of 1. As shown in Figure 10a, the yellow line indicates defect location 1 on the positioned feature map. Figure 10b displays the original grayscale distribution at location 1, while Figure 10c shows the grayscale distribution after filling the concave segment at location 1. After the filling, the grayscale profile becomes unimodal. Subsequently, concave segments with a width of 2 are filled in the same manner, and so on.

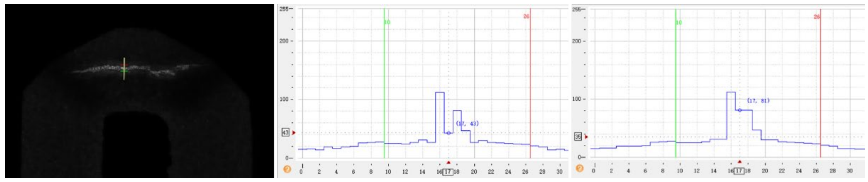

a Defect location b Original grayscale distribution c Grayscale profile after filling

Figure 10. Results of concave segment filling.

Let the grayscale function of a one-dimensional grayscale defect along the X or Y axis of the image be represented by the grayscale value at point i. First, the background is determined using the absolute magnitude. Since the feature map is a normalized image, the defect region often exhibits significantly higher grayscale values, approximately 5-10 times the background grayscale. Therefore, the threshold for the background is set as twice the average value of the current grayscale line. When the absolute magnitude exceeds this background threshold, extremal points are marked. If $f(i) > f(i-1)$ and $f(i) > f(i+1)$, then $f(i)$ is local maxima, and the pixel is marked accordingly. When the width of the convex segment is 2, If $f(i) > f(i-1)$, $f(i) = f(i+1)$ and $f(i) > f(i+2)$, then both $f(i)$ and $f(i+1)$ are local maxima, Only mark $f(i)$. As shown in Figure 5.11a, the feature map after ROI localization. In Figure 11, the red pixels indicate the results of marking extreme points along the Y direction.

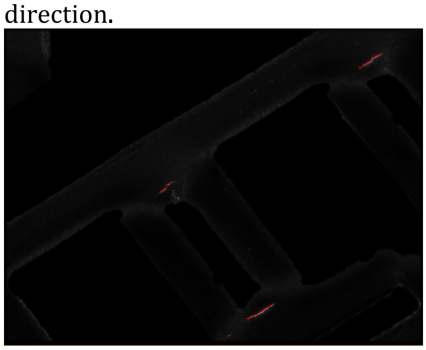

Figure 11. Results of marking extreme points along the Y-axis.

If the marking is only along the grayscale line in one direction, when the defect is aligned with that direction, if the defect is marked only along the X direction, the marking may be much smaller than the length of the defect. Therefore, in this paper, markings are performed separately along the X and Y directions, and then convolution is used in both directions to remove discrete points. Finally, the markings from both directions are combined to obtain the merged marking result.

a. Marking result along the X-axis b. Marking result along the Y-axis

Figure 12. Comparison before and after removing discrete point interference along the X-axis.

To ensure the robustness of the algorithm, the threshold used to eliminate background noise is set low. As a result, the change in curvature at the junction of the inclined planes may not be fully removed, leading to discrete extreme points. If extreme points are directly used to identify defects, false detections may occur. Since the extreme points of defects are not isolated, while noise points are usually isolated, this paper removes the extreme points that do not belong to the defect by calculating the number of surrounding marked points for each labeled point. The number of extreme points within the neighborhood is computed using convolution.

As shown in Figure 13, using a 3×3 convolution kernel as an example, a kernel with all elements set to 1 is convolved with the labeled image to obtain the number of labeled points within the neighborhood of each marked point. If the number of labeled points in the neighborhood is less than the radius of the convolution kernel (the width in the figure is 2), the marked point is removed.

The final result after removing discrete points using the convolution kernel is shown in Figure 14, where the stamping defect on the corrugated board is effectively detected.

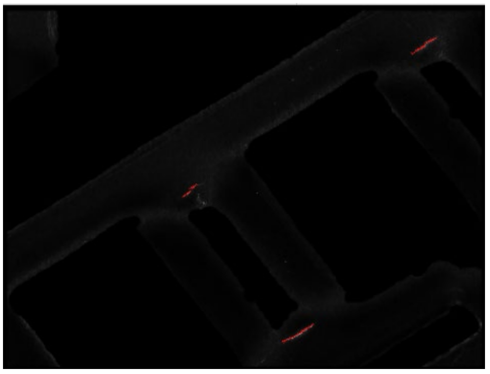

Figure 14. Final marking result

3. Experiment and Result Analysis

Tests were conducted on three different models of corrugated boards (EA10B, U10B, and U15N). The hardware system designed for this experiment was used to capture images of the heat exchange area and the flow diversion area of these three corrugated board models.

The heat exchange area structures of the three models are similar and relatively simple, all forming a V-shaped structure composed of corrugated inclined surfaces in two orientations, as shown in Table 2. For each model and each orientation, 50 sets of photometric stereo data were captured, and 50 sets of photometric stereo data were collected at the junction. Table 3 lists the specific numbers of concave and convex patterns.

Table 2. Heat exchange zone dataset

Model	Heat Exchange Zone Inclined Surface	Inclined Surface Junction
EA10B	100Sets	50Sets
U10B	100Sets	50Sets
U15N	100Sets	50Sets

Table 3. Number of diversion zone patterns for each model

Model	B-Pattern	T-Pattern
EA10B	122pieces	100pieces
U10B	156pieces	154pieces
U15N	226pieces	274pieces

To ensure that each pattern appears completely at least once in the field of view, the flow diversion area of these three models was photographed 194, 242, and 263 times, respectively. As shown in Table 4, a total of 194, 242, and 263 sets of photometric stereo data were collected for these three models.

Table 4. Diversion zone dataset

Model	Numbers	B-Pattern	T-Pattern
EA10B	194 Sets	436 pieces	445 pieces
U10B	242 Sets	327 pieces	322 pieces
U15N	263 Sets	679 pieces	651 pieces

Among them, the flow diversion area of the corrugated board contained a total of 44 defective sets of data, with 62 defects in the field of view. The images without defects totaled 655 sets. For the heat exchange area, each model's corrugated surface orientation was captured 100 sets, and 50 sets at the corrugated junction, for a total of 450 sets of images. Among them, 38 sets were defective images, with 40 defects in the field of view, and 412 sets of images without defects.

The defect detection performance is evaluated using three parameters: missed detection rate, false detection rate, and accuracy. The missed detection rate (FNR) is defined as:

$$FNR = \frac{FN}{FN + TP}$$

The false positive rate (FPR) is defined as:

$$FPR = \frac{FP}{FP + TN}$$

The accuracy (ACC) is defined as:

$$ACC=\frac{TP+TN}{FN+TP+FP+TN}$$

In this context, FN refers to the number of defective images that were not detected.TP refers to the number of defective images correctly identified as containing defects. FP refers to the number of non-defective images incorrectly identified as containing defects.TN refers to the number of non-defective images correctly identified as defect-free. The accuracy of defect detection is shown in Table 5.

Table 5. Defect detection dataset

Location	Non-defective Feature Map	Defective Feature Map	Total Number
Diversion zone	655	44	699
Heat Exchange zone	412	38	450

4. Summary

The corrugated board, as one of the representatives of complex metal surfaces, presents a challenge for rapid and high-precision defect detection due to factors such as surface complexity and the special reflective properties of metal surfaces. This remains a challenging problem in industrial manufacturing and quality control. This paper, based on the principles of camera imaging and photometric stereo vision, proposes a framework for detecting stamping defects on corrugated boards. The research not only has significant practical importance for defect detection of corrugated boards and ensuring the quality of heat exchangers, but also provides a theoretical foundation for the three-dimensional detection methods of complex surfaces that can be applied to other metal parts. This research is scientifically meaningful for addressing defect detection issues in machine vision for surfaces with complex topography.

References

[1] Mahmoudinezhad S, Sadi M, Ghiasirad H, et al. A comprehensive review on the current technologies and recent developments in high-temperature heat exchangers[J]. Renewable and Sustainable Energy Reviews, 2023, 183: 113467.

[2] Qiu, B., Chen, S., Wang, Y., Li, K., Wang, X., & Sun, Y. (2022). Analysis of defect causes and improvement suggestions for nuclear island plate heat exchangers. Industry and Technology Forum, 21(04), 36-38.

[3] Li D, Xu J, Zhang Y, et al. Blocky corrugations recognition based on graph theory for corrugated sheets of plate heat exchanger[J]. Measurement, 2023, 221: 113588.

[4] Weber M, Cipolla R. A Practical Method for Estimation of Point Light-Sources[J]. Proceedings Bmvc, 2003.

[5] Liu H, Wu X, Yan N, et al. A novel image registration-based dynamic photometric stereo method for online defect detection in aluminum alloy castings[J]. Digital Signal Processing, 2023, 141: 104165.

[6] Deng, X. Design and implementation of a surface 3D reconstruction system based on photometric stereo vision. Guangdong University of Technology.

[7] Horn B K P. Obtaining shape from shading [J]. Psychology of Computer Vision, 1975, 2(1): 115-155.

[8] Woodham R J. Photometric Method for Determining Surface Orientation from Multiple Images[J]. Optical Engineering, 1992, 19(1).

[9] Huo, N., Wang, L., & Jiang, X. Machine Vision. China Youth Publishing House, 242-243.

[10] Yuan, W. Image segmentation method based on directional space: CN112446894A. March 5, 2021.